Robust single-particle tracking in live-cell time-lapse sequences

Khuloud Jaqaman[1], Dinah Loerke[1], Marcel Mettlen[1], Hirotaka Kuwata[2], Sergio Grinstein[2], Sandra L Schmid[1] & Gaudenz Danuser[1]

Single-particle tracking (SPT) is often the rate-limiting step in live-cell imaging studies of subcellular dynamics. Here we present a tracking algorithm that addresses the principal challenges of SPT, namely high particle density, particle motion heterogeneity, temporary particle disappearance, and particle merging and splitting. The algorithm first links particles between consecutive frames and then links the resulting track segments into complete trajectories. Both steps are formulated as global combinatorial optimization problems whose solution identifies the overall most likely set of particle trajectories throughout a movie. Using this approach, we show that the GTPase dynamin differentially affects the kinetics of long- and short-lived endocytic structures and that the motion of CD36 receptors along cytoskeleton-mediated linear tracks increases their aggregation probability. Both applications indicate the requirement for robust and complete tracking of dense particle fields to dissect the mechanisms of receptor organization at the level of the plasma membrane.

With the development of bright fluorescent probes, stable microscopes and sensitive cameras, live-cell imaging has become a standard technique to study subcellular dynamics. The resulting images often consist of punctate features, representing small molecular assemblies or even single molecules[1–3]. To study the molecular mechanisms that drive the observed dynamics, such experiments must be combined with SPT, which captures the full spatiotemporal complexity of subcellular particle behavior.

SPT faces several challenges that in practice hinder such studies. Notably, SPT goes beyond the detection and localization of particles; its key step is the establishment of correspondence between particle images in a sequence of frames. Establishing correspondence is complicated by various factors, most notably by high particle density, particle motion heterogeneity, temporary particle disappearance (for example, owing to out-of-focus motion and detection failure), particle merging (two particles approaching each other within distances below the resolution limit) and particle splitting (two unresolved particles diverging to resolvable distances)[4,5]. Previously many of these challenges have been overcome by diluting the fluorescent probes, which resulted in a low particle density with almost unambiguous particle correspondence[6,7]. Under such conditions, particle tracking is indeed reduced to a simple particle detection and localization problem[8]. However, although analysis of samples with low particle densities reveals motion characteristics[1–3,9,10], analysis of such samples does not allow probing of the interactions between particles[11]. Also, the amount of data collected per experiment is low, limiting the observation of spatially and temporally heterogeneous particle behavior and hindering the capture of infrequent events. Furthermore, even with low particle density, low signal-to-noise ratio (SNR) and probe flicker complicate the search for particle correspondence. Therefore, for most cell biological studies, there is a great need for robust SPT methods that address the challenges mentioned above.

The most accurate solution to SPT is provided by the method of multiple-hypothesis tracking (MHT)[12]. In MHT, given particle positions in every frame, all particle paths within the bounds of expected particle behavior are constructed throughout an entire movie. The largest nonconflicting ensemble of paths is then chosen as the solution, where nonconflicting means that no two paths share in any frame the image of the same particle. This solution is globally optimal in both space and time, that is, it is the best solution that can be found by simultaneously accounting for all particle positions at all time points. Clearly, MHT is computationally prohibitive even for problems with a few tens of particles tracked over a few tens of frames. Therefore, heuristic algorithms with higher computational efficiency have been proposed to approximate the MHT solution. Most of these algorithms are greedy, that is, they seek to approach the globally optimal solution by taking many locally optimal solutions. Usually, this means that particle correspondence is determined step by step between consecutive frames[13], reducing computational complexity at the expense of temporal globality. Many tracking algorithms then solve the frame-to-frame correspondence problem in a spatially global manner[14–20] and seek to recover tracks after temporary particle disappearance[14–18,21]. Some algorithms treat merging and splitting as a temporary disappearance of one of the particles[14–16], whereas others treat them as separate events[20,22]. One approach to SPT is unique in that it uses kymograms

[1]Department of Cell Biology, The Scripps Research Institute, 10550 N. Torrey Pines Rd, La Jolla, California 92037, USA. [2]Department of Cell Biology, The Hospital for Sick Children, 555 University Ave., Toronto M5G1X8, Canada. Correspondence should be addressed to K.J. (kjaqaman@scripps.edu).

RECEIVED 26 FEBRUARY; ACCEPTED 18 JUNE; PUBLISHED ONLINE 20 JULY 2008; DOI:10.1038/NMETH.1237

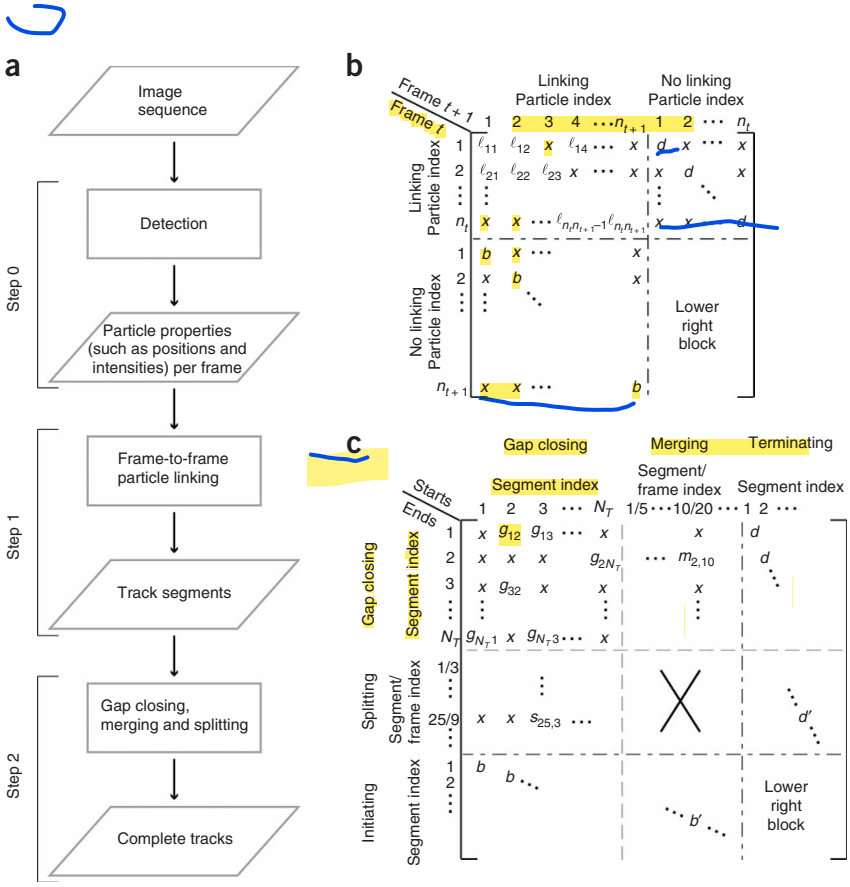

Figure 1 | Tracking particles via spatially and temporally global assignments. (**a**) Tracks were constructed from an image sequence by detecting particles in each frame (step 0), linking particles between consecutive frames (step 1) and then closing gaps and capturing merging and splitting events between the initial track segments (step 2). (**b**) Cost matrix controlling particle assignments between frames. ℓ_{ij}, cost for linking particle i in frame t to particle j in frame $t + 1$; x, impossible link whose cost exceeded the cutoff; d, cost for allowing particles in frame t to link to nothing in frame $t + 1$; b, cost for allowing particles in frame $t + 1$ to get linked by nothing in frame t. The lower right block is an auxiliary block required to satisfy the topological constraints of the LAP (**Supplementary Note 3**). (**c**) Cost matrix controlling gap closing, merging and splitting. g_{IJ}, cost for closing a gap between the end of track segment I and the start of track segment J; m_{IJ}, cost for the end of track segment I merging with a middle point of track segment J; s_{IJ}, cost for the start of track segment J splitting from a middle point of track segment I. X in the center, links between track segment middle points introduced for merging and splitting were not allowed. The upper and middle right blocks, lower left and middle blocks, and lower right block were as described in **b**. In **b** and **c**, "…" indicates index continuation.

to maximally benefit from temporal information and thus avoid many of the problems of greedy algorithms[23]. However, this method cannot be used to track Brownian motion and is thus not generally applicable. Although the many existing algorithms address one or the other of the issues in SPT, none of them tackle all the issues simultaneously. Consequently, investigators must sacrifice some tracking aspects for the sake of others, based on their specific application.

Here we present a tracking algorithm that uses one mathematical framework, the linear assignment problem (LAP)[24,25], to provide an accurate solution to all the SPT challenges listed above. Given a set of detected particles throughout a time-lapse image sequence, the algorithm first links the detected particles between consecutive frames, and then links the track segments generated in the first step to simultaneously close gaps and capture particle merge and split events. Thus, although the initial particle assignment is temporally greedy, the subsequent track segment assignment is accomplished via temporally global optimization, overcoming the shortcomings of algorithms relying solely on greedy assignment strategies. Both steps use global optimization in space. Overall, this approach defines an accurate, yet computationally feasible, approximation to MHT, allowing the robust tracking of particles under high-density conditions.

We demonstrate our approach based on two applications that critically depend on tracking robustness and globality: (i) accurate, comprehensive lifetime analysis of endocytic clathrin-coated pits (CCPs) and (ii) single-molecule tracking of the macrophage transmembrane receptor CD36, revealing receptor aggregation and dissociation events.

RESULTS

Tracking via spatially and temporally global assignments

Given the set of detected particles in a live-cell time-lapse sequence (**Supplementary Notes 1** and **2** online present the detection algorithms used for the two applications shown in this work and their performance), we generated particle tracks in two steps (**Fig. 1a**). First, we constructed track segments by linking the detected particles between consecutive frames, under the condition that a particle in one frame could link to at most one particle in the previous or the following frame. These track segments started and ended not only because of the true appearance and disappearance of particles, but also because of apparent disappearances owing to noise and limitations in imaging, for example, when a particle temporarily moved out of the plane in focus or when two particles approached each other within a distance smaller than the resolution limit. The track segments obtained in this step tended to be incomplete, resulting in a systematic underestimation of particle lifetimes. In addition, because of the one-to-one assignment of particles, this step could not capture particle merges and splits, which by definition required one particle in one frame to be assigned to two particles in the previous or subsequent frame, respectively. Therefore, in a second step, we linked the initial track segments in three ways: (i) end to start, to close gaps resulting from temporary disappearance, (ii) end to middle, to capture merging events, and (iii) start to middle, to capture splitting events.

We formulated both the frame-to-frame particle linking step and the gap closing, merging and splitting step as LAPs[24,25]. In the LAP framework, every potential assignment (particle assignment in the first step, track segment assignment in the second step) was

characterized by a cost C (matrix entries in **Fig. 1b,c**). The goal of solving the LAP in each step was then to identify the combination of assignments with the minimal sum of costs:

$$\hat{A}_{\arg\min} = \sum_{i=1}^{\text{Number of rows}} \sum_{j=1}^{\text{Number of columns}} A_{ij}C_{ij}, \quad (1)$$

such that

$$\sum_{i=1}^{\text{Number of rows}} A_{ij} = 1 \quad \text{and} \quad \sum_{j=1}^{\text{Number of columns}} A_{ij} = 1. \quad (2)$$

In equation 1, A is any assignment matrix with entries 1 (link) and 0 (no link), and $\hat{A}$ is the assignment matrix that minimizes the sum of costs. The conditions on A (and consequently $\hat{A}$) in equation 2 guaranteed that the selected assignments were mutually exclusive, that is, no particle or track segment could be included in more than one assignment. Thus, when a particle or track segment had multiple potential assignments, the assignments competed with one another. Although assignments with a lower cost tended to win, the requirement for a globally minimized cost could result in the selection of assignments in which the costs were not the lowest.

In the frame-to-frame particle linking step, three types of potential assignments were in competition (**Fig. 1b**). A particle in the source frame t could link to a particle in the target frame $t + 1$ (cost function ℓ). Alternatively, a particle in the source frame could link to nothing, leading to a track segment end (cost function d), or a particle in the target frame could get linked by nothing, leading to a track segment start (cost function b). The decision between these possibilities was made globally in space (equations 1 and 2). However, the assignment was temporally greedy as it was based on particle configuration in the specific source and target frames only.

In the gap closing, merging and splitting step, six types of potential assignments were in competition (**Fig. 1c**). The end of a track segment could link to the start of another track segment, thus closing a gap (cost function g), the end of a track segment could link to a middle point of another track segment, leading to a merge (cost function m), or the start of a track segment could get linked by a middle point of another track segment, leading to a split (cost function s). Alternatively, the end of a track segment could link to nothing, leading to a track termination (cost function d), the start of a track segment could get linked by nothing, leading to a track initiation (cost function b), or the track segment middle points introduced for merging and splitting could link to nothing, refusing a merge or a split (cost functions d' and b'). In this step, all track segments throughout the entire movie competed with each other. Thus, the LAP solution (equations 1 and 2) was global in both space and time.

The framework described up to this point is general. Its goal is to provide a robust yet computationally feasible approximation to MHT. It is independent of the actual cost functions used to weigh the various competing assignments. Thus, it is independent of problem dimensionality (we solved two- and three-dimensional tracking problems with the same framework; data not shown) as well as of the type of particle motion (Brownian motion and directed motion, among others). It is also independent of the physical nature of the particle (single molecule, molecular assembly, organelle and others), which mainly influences the choice of an appropriate particle-detection method.

The cost functions, in contrast, must be tailored to the specific tracking application. In our implementation, we technically solved this by treating the cost functions themselves as input variables together with their parameters. Here we demonstrate the definition of cost functions for tracking isotropic random motion, such as pure or confined Brownian motion, owing to its prevalence in cell biological applications. In this case, the costs for linking (ℓ), gap closing (g), merging (m) and splitting (s) were functions of distance and intensity:

$$\ell_{ij} = \delta_{ij}^2, \quad (3)$$

$$g_{IJ} = \delta_{IJ}^2, \quad (4)$$

$$m_{IJ}, s_{IJ} = \begin{cases} \delta_{IJ}^2 \times \rho_{IJ}, & \rho_{IJ} > 1 \\ \delta_{IJ}^2 \times \rho_{IJ}^{-2}, & \rho_{IJ} < 1 \end{cases}. \quad (5)$$

In equation 3, δ_{ij} is the distance between particles i and j. In equation 4, δ_{IJ} is the distance between the end of track segment I and the start of track segment J. In equation 5, δ_{IJ} is the distance between the end or start of track segment I and the middle point of track segment J, and ρ_{IJ} is the ratio of the intensities A_I (of track segment I) and A_J (of track segment J) before and after merging or splitting:

$$\rho_{IJ}(\text{merge in frame } t) = \frac{A_J(t)}{A_I(t-1) + A_J(t-1)},$$
$$\rho_{IJ}(\text{split in frame } t) = \frac{A_J(t-1)}{A_I(t) + A_J(t)}. \quad (6)$$

The intensity factor increased the cost when the intensity after merging or before splitting was different from the sum of intensities before merging or after splitting, with a higher penalty when the intensity was smaller. This intensity penalty ensured that merging and splitting events were not picked up only because of the proximity of particle tracks but that the associated intensity changes were consistent with the image superposition of merging or splitting particles. The alternative costs used to reject particle linking, gap closing, merging and splitting (b, b', d, d' in **Fig. 1b,c**) are described in **Supplementary Note 3** online.

To exclude physically nonsensical solutions, in practice we did not allow every particle or track segment to potentially link to every particle or track segment, but rather introduced cutoffs that excluded impossible links a priori (x in **Fig. 1b,c**). For frame-to-frame particle linking and for gap closing, we based the cutoff on distance. For merging and splitting, we based the cutoff on both distance and intensity. Distance-based cutoffs were data-driven: they were derived for every particle from its observed motion, allowing for self-adaptation (**Supplementary Note 3**).

Validation of tracking algorithm on simulated tracks

We validated our algorithm by tracking simulated particles at different densities and with different signal stability. The particle density and signal stability used in the simulations were varied from conditions similar to the experimental data (**Supplementary Table 1** online) to much harsher conditions, the purpose of which

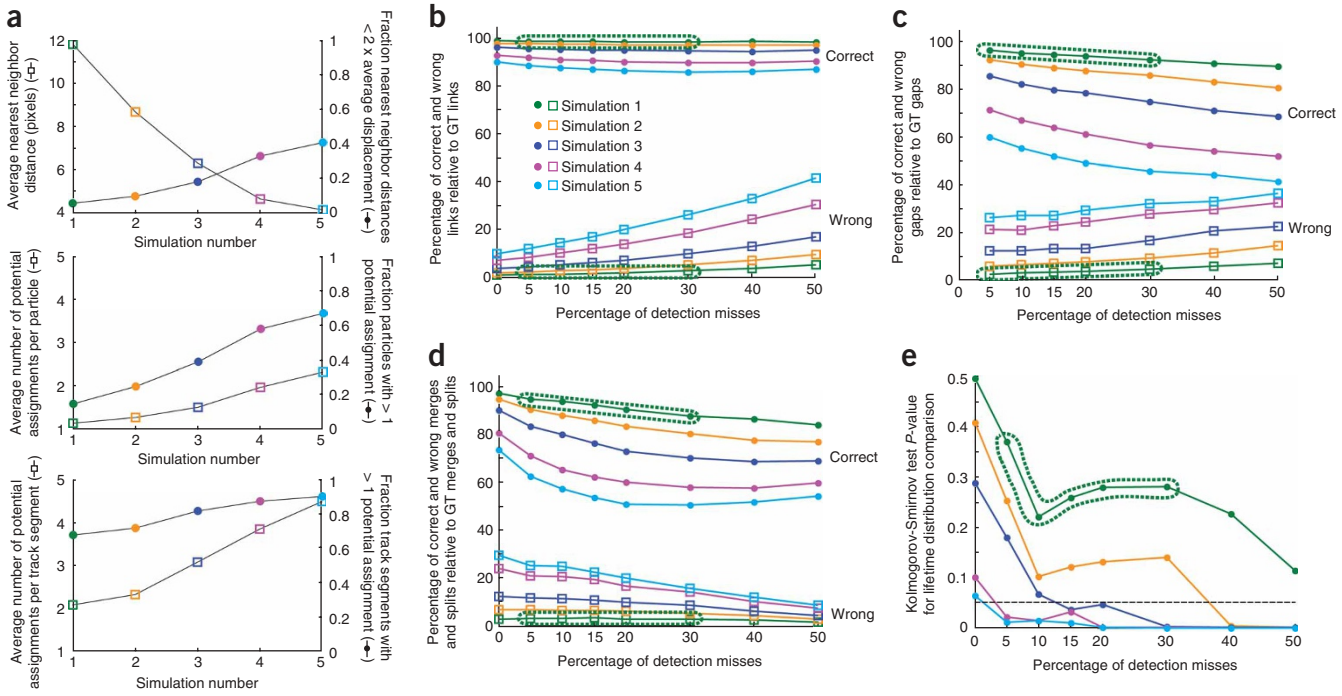

Figure 2 | Validation of tracking algorithm on simulated tracks. (**a**–**e**) Five simulations of increasing particle density, each combined with eight detection efficiencies represented by percentages of particles missing from the detection, were used to test the performance of the tracking algorithm. The results shown are the averages over 6 repetitions of each simulation. Criteria to assess particle density in simulation as related to tracking (**a**). Top and middle panels evaluated at 0% detection misses. Bottom panel evaluated at 20% detection misses (at 0% misses, there are no gaps to close). Percentage of true and false positives in particle linking (**b**), gap closing (**c**) and merging and splitting (**d**) relative to GT. *P*-value of the Kolmogorov-Smirnov test comparing the measured and GT lifetime distributions (**e**). The 0.05 significance threshold is indicated by a dashed line. Conditions similar to the experimental data are highlighted with a dotted outline.

was to identify the breakdown of the method. Simulated particles moved in a Brownian fashion ($D = 0.75$ pixels^2/frame corresponding to an average displacement between frames of 1.7 pixels, similar to the average displacement observed for CD36 receptors and CCPs), underwent merge and split events, and their lifetimes followed a Rayleigh distribution (chosen to reflect the maturation process of molecular aggregates such as CCPs). We varied particle density by gradually decreasing the average nearest neighbor distance from 12 to 4 pixels, corresponding to 6–42% of particles having nearest neighbors that were closer than twice their average displacement between frames (**Fig. 2a**). Under these conditions, particles and track segments had on average more than one potential assignment in their respective linking steps, with the number of potential assignments increasing with particle density (**Fig. 2a**). The tracking of particles under these high density conditions required a global optimization approach that can resolve assignment ambiguities and conflicts.

To test the performance of the tracking algorithm independently of the detection algorithm, we simulated trajectories (ground truth; GT) and directly derived from them a list of particle positions and intensities per frame. We accounted for the effect of signal stability on detection by deleting a fraction of the particles from the list, in which a lower signal stability (for example, because of lower SNR) led to a larger fraction being deleted (**Supplementary Notes 1** and **2** show the relationship between SNR and the fraction of particles missed by the detection algorithms used). For the validation process, we varied the fraction of particles missed by the detection algorithm from 0 to 50%. We did not include false detection positives in the validation process because in practice false positives tended to have very short trajectories (2–3 frames long), which could be identified and removed from the ensemble of trajectories a posteriori.

We evaluated the tracking results in terms of the fraction of true positive and false positive links, closed gaps and merging and splitting events, relative to the GT (**Fig. 2b–d**). As expected, the tracking algorithm performed best for the lowest-density simulation with 0% detection misses, and its performance decreased almost monotonically with increasing particle density and increasing detection misses. Under all tested conditions, there were more correct links, gaps, merges and splits than wrong ones. Notably, even at the highest density (simulation 5, 0% misses), where ~40% of particles had nearest neighbors closer than twice their average displacement, there were only 10% false links, demonstrating the power of a global tracking approach.

We also evaluated the tracking results in terms of the particle lifetime distribution, which we compared to the GT lifetime distribution via the Kolmogorov-Smirnov test (**Fig. 2e** and **Supplementary Note 4** online). Lifetime measurements rely on all aspects of tracking and thus are the most sensitive to tracking errors. Any mistakes in the particle linking or gap closing steps break up particle trajectories, resulting in the systematic underestimation of particle lifetimes. Therefore, the comparison of simulated and retrieved particle lifetime distributions was the most comprehensive performance measure for tracking. This

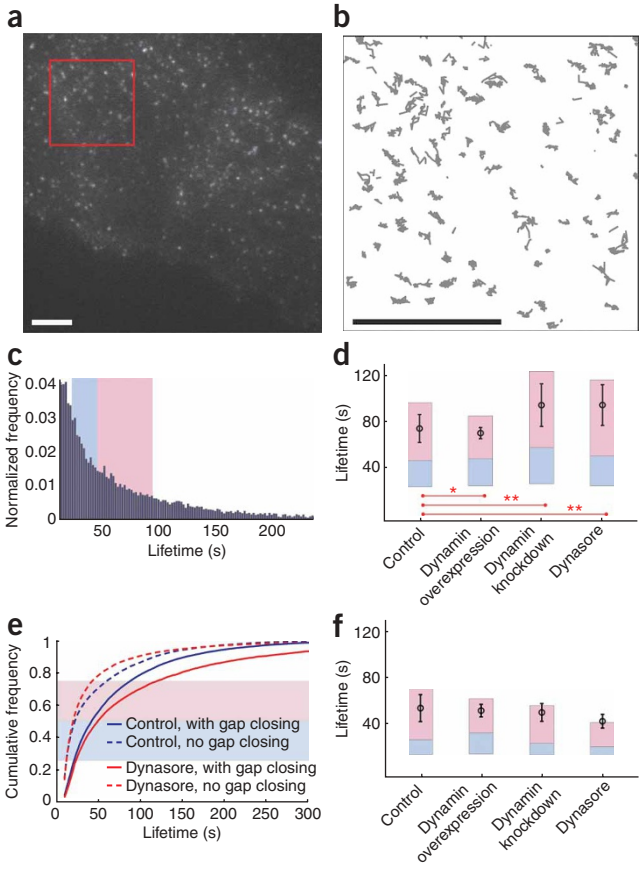

Figure 3 | CCP lifetime is regulated by dynamin. (**a**) TIRF microscopy image of a BSC1 cell fluorescently labeled with clathrin light chain–EGFP. Scale bar, 5 μm. (**b**) CCP trajectories in the 10 × 10 μm area indicated by a red box in **a**. (**c**) Normalized lifetime histogram of 21,518 CCP trajectories pooled from 11 control cell movies. Shaded blue and pink areas: second and third data quartiles. (**d**) CCP lifetimes for control and for alterations of dynamin function. Blue and pink bars, second and third data quartiles. Error bars, cell-to-cell s.d. (calculated for 11 control, 4 dynamin overexpression, 15 dynamin knockdown and 5 dynasore) of the mean (circles). $*P < 10^{-5}$, $**P < 10^{-10}$ (Kolmogorov-Smirnov test). (**e**) Cumulative frequency of CCP lifetimes in control and dynasore-treated cells, resulting from tracking with gap closing (as in **b**–**d**) and without gap closing. (**f**) CCP lifetimes for control and for alterations of dynamin function resulting from tracking without gap closing.

comparison indicated that robust tracking required a trade-off between particle density and signal stability. As the particle density increased, less detection misses could be tolerated (that is, higher signal stability was required): At the lowest density, tracking was reliable even with 50% detection misses; with no detection misses, tracking was reliable up to the highest density.

CCP lifetime is regulated by dynamin

We used our tracker to assay the lifetime of endocytic CCPs in BSC1 cells expressing a fully functional clathrin light chain–enhanced GFP (EGFP) construct[26] (**Fig. 3a**). CCP dynamics can be visualized at high time resolution by total internal reflection fluorescence (TIRF) microscopy[27]. However, it has remained a challenge to extract reliable lifetime data from TIRF microscopy movies, as lifetime measurements are notoriously susceptible to tracking errors, as caused, for example, by the temporary loss of the fluorescence signal of a CCP or by ambiguity in the assignment of CCP images between consecutive frames. As a result, tracking has previously been accomplished either manually for a low number of well-discernable CCPs[27,28] or using semi-automated tracking restricted to isolated and bright CCPs that do not have close neighbors that can potentially confuse the tracking algorithm[26,29].

We detected CCPs using a method based on the *à trous* wavelet decomposition[30] (**Supplementary Note 1**). Because of the globality and gap closing feature of our tracker, we could extract complete CCP tracks independent of their brightness and position relative to other CCPs (**Fig. 3b** and **Supplementary Video 1** online). We verified that our gap closing maximized the retrieval of tracks interrupted by temporary particle disappearance while minimizing the erroneous linking of true track terminations to true track initiations by analyzing the distribution of gap lengths identified by our tracker (**Supplementary Fig. 1** online). First, longer gaps were less abundant than shorter gaps, indicating that the time window of eight frames we chose for gap closing captured most gaps in the system, preventing the systematic underestimation of CCP lifetimes. Second, the distribution of gap lengths, expressed in frames, was independent of frame rate (0.5 Hz vs. 2.5 Hz), demonstrating that the gaps closed resulted from detection failure in the noisy images. In contrast, the erroneous linking of true track terminations to true track initiations would have lead to a gap length distribution that exhibited a characteristic time scale expressed in seconds, resulting in systematic differences between the gap length distributions expressed in frames.

We measured CCP lifetimes in control cells and in cells in which the function of dynamin, a key component of the endocytic machinery[31], was altered (**Fig. 3c**,**d**). Overexpression of wild-type dynamin decreased the mean CCP lifetime, whereas dynamin knockdown with small interfering RNA increased the mean lifetime. Treatment of cells with dynasore, a small-molecule inhibitor of dynamin[32], also increased the average lifetime. Notably, the third quartiles of the lifetime distributions changed more dramatically than the second quartiles, suggesting that dynamin might differentially affect short and long-lived CCP subpopulations. We explored these behaviors in more detail elsewhere (D.L., M.M., D. Yarar, K.J., H. Jaqaman, G.D. and S.L.S., submitted manuscript). Notably, the differentiation between these lifetime histograms critically depended on the application of temporally global gap closing. For example, while proper gap closing revealed that the treatment of cells with dynasore increased CCP lifetimes, tracking without gap closing resulted in an apparent decrease in CCP lifetimes (**Fig. 3e**,**f**), owing to the lower stability of CCP signals upon dynasore treatment. Thus, tracking without gap closing resulted in lifetime distributions that were simply a reflection of the breakage of tracks due to limited SNR, masking away the effects of dynamin on CCP maturation kinetics.

CD36 receptor aggregation activity depends on motion type

We also used our tracker to follow the motion of the macrophage transmembrane receptor CD36 and to characterize the aggregation state of individual surface bound CD36 molecules. At rest, CD36 is thought to exist as quiescent monomers, which are activated and internalized in response to oligomerization by multivalent ligands like oxidized LDL and malaria-infected red blood cells[33]. However, we found that CD36 resided predominantly in multi-molecular

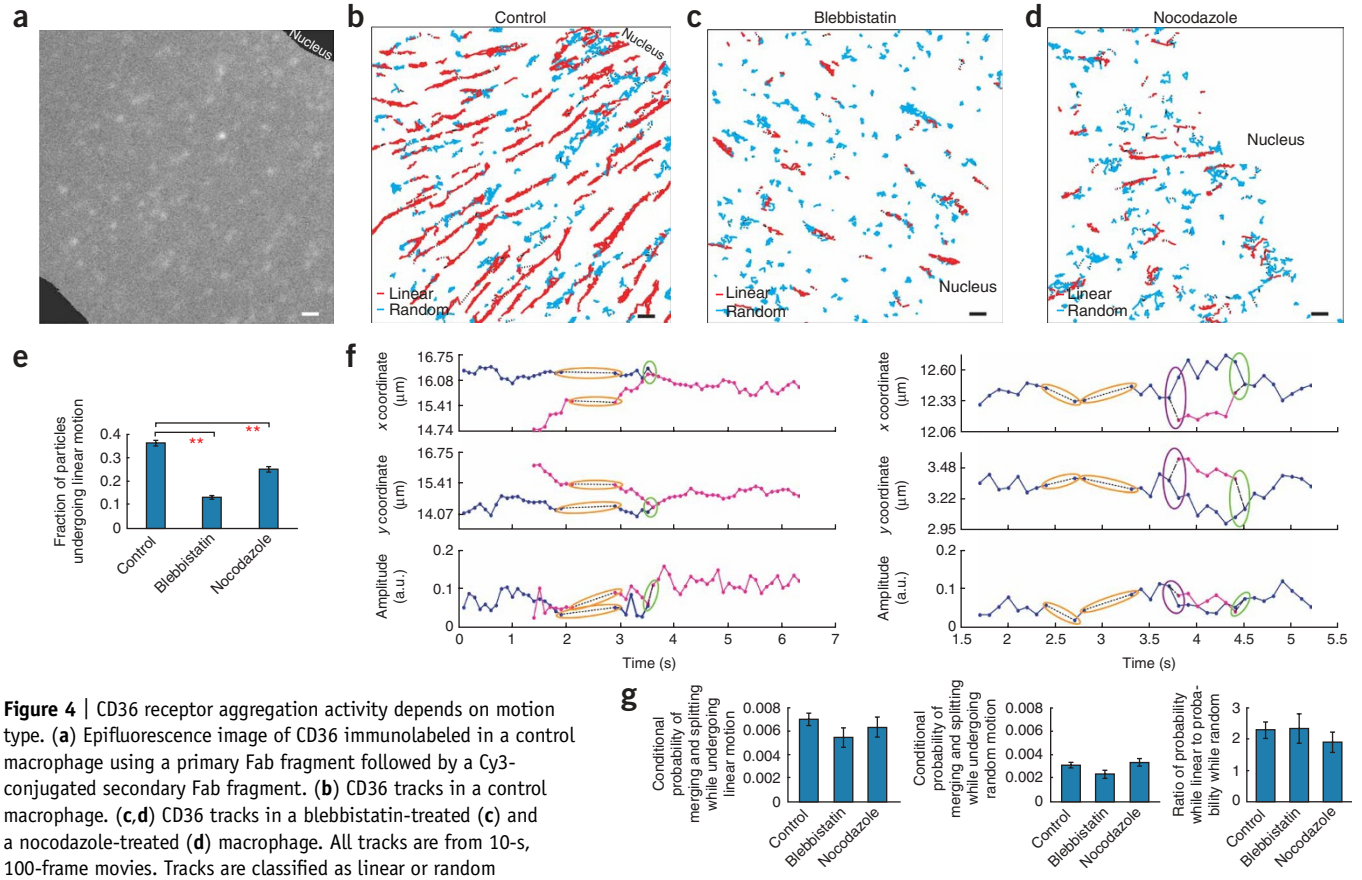

Figure 4 | CD36 receptor aggregation activity depends on motion type. (**a**) Epifluorescence image of CD36 immunolabeled in a control macrophage using a primary Fab fragment followed by a Cy3-conjugated secondary Fab fragment. (**b**) CD36 tracks in a control macrophage. (**c**,**d**) CD36 tracks in a blebbistatin-treated (**c**) and a nocodazole-treated (**d**) macrophage. All tracks are from 10-s, 100-frame movies. Tracks are classified as linear or random (**Supplementary Note 6**). Scale bars, 1 μm. (**e**) Fraction of particles undergoing linear motion. (**f**) Two sample trajectories represented as *x* coordinate, *y* coordinate and amplitude over time, highlighting merging events (green ovals), splitting events (purple ovals) and closed gaps (orange ovals). Two track segments (blue and magenta) are brought together by capturing merge and split events. (**g**) Conditional probabilities of merging and splitting while undergoing linear motion and while undergoing random motion, and ratio of conditional probability while undergoing linear motion to conditional probability while undergoing random motion. In **e** and **g**, error bars indicate s.d. as calculated from a sample of size 200 generated by the bootstrap method. $^{**}P < 10^{-10}$. Statistics were calculated from 14 control cells (7,527 trajectories $\geq$ 5 frames long), 11 blebbistatin-treated cells (5,148 trajectories $\geq$ 5 frames long) and 12 nocodazole-treated cells (4,926 trajectories $\geq$ 5 frames long). Trajectories shorter than 5 frames were excluded as nonclassifiable with respect to motion type.

complexes containing several copies of the receptor (intensity analysis of single-molecule movies of CD36; K.J., H.K., N. Touret, W. Trimble, G.D. and S.G., manuscript in preparation). The ability of our tracker to capture merging and splitting events enabled us to determine whether the observed CD36 aggregates were stable or instead underwent dissociation and re-association.

We immunolabeled surface-bound CD36 receptors in primary macrophages by a primary Fab fragment and a Cy3-conjugated secondary Fab fragment and recorded single-molecule movies using epifluorescence microscopy at a frame rate of 10 Hz (**Fig. 4a** and **Supplementary Video 2** online). Both individual receptors and receptor aggregates generated diffraction-limited image features. Thus, we estimated particle positions by first detecting local maxima and then fitting Gaussian kernels in areas around these local maxima to achieve subpixel localization[34]. To enhance detection efficiency under the low SNR conditions of single-molecule movies, we performed the search for local maxima in time-averaged images, followed by Gaussian kernel fitting in individual frames (**Supplementary Note 2** and **Supplementary Video 2**).

A substantial subset of surface-bound CD36 receptors and receptor aggregates moved along linear tracks that radiated from the perinuclear region (**Fig. 4b**, **Supplementary Video 3** and **Supplementary Notes 5** and **6** online). The molecules moving along linear tracks took larger steps (both forward and backward) along the preferred direction of motion than perpendicular to it. To accurately track both subsets of CD36 molecules, those moving randomly and those moving along linear tracks, we modified the cost functions of equations 3–6 such that particles with significant evidence for motion along linear tracks could benefit from an explicit linear motion model (**Supplementary Note 7** online describes the modified cost functions and illustrates the shortcomings of tracking CD36 molecules with the random motion model of equations 3–6; **Supplementary Fig. 1** shows detailed statistics on the recovered gaps, merges and splits in CD36 tracks).

Owing to the radial arrangement of the linear CD36 tracks, we suspected that the linear component of CD36 motion was dependent on actomyosin-driven flow of the cortical network and/or on microtubule-guided motors or diffusion. To test this hypothesis, we treated macrophages with either blebbistatin

to inhibit myosin II activity or nocodazole to depolymerize microtubules. Blebbistatin (10 μM for 10 min) stopped the linear motion almost completely (**Fig. 4c** and **Supplementary Video 3**). Nocodazole (50 μM for 30 min) also reduced the linear motion, but to a lesser extent (**Fig. 4d** and **Supplementary Video 3**). The decrease in the fraction of particles undergoing linear motion was significant in both cases (**Fig. 4e**; *t*-test $P < 10^{-10}$). These results imply that the linear component of CD36 motion may depend on receptor engagement with both microtubules and cortical actomyosin. They also illustrate the ability of the tracker to distinguish random motion from linear motion: inclusion of an explicit linear motion model did not generate artificial linear tracks under drug perturbations.

Under all conditions, the CD36 receptors and receptor aggregates underwent merging and splitting events (in **Fig. 4f** we highlighted two examples of merging and splitting particles, which illustrate the strong geometric and intensity cues for merge and split events). We calculated the conditional probability of particles merging and splitting while undergoing linear motion versus the conditional probability of merging and splitting while undergoing random motion (**Fig. 4g**; in **Supplementary Note 8** online we discuss the conditional probability analysis). For control as well as drug-perturbation experiments, the conditional probability of merging and splitting while undergoing linear motion was about two times higher than the conditional probability while undergoing random motion. This implies that CD36 receptors moving along linear tracks aggregated and dissociated about twice as often as CD36 receptors not moving along linear tracks. Notably, there were no significant differences between control and drug perturbation experiments in terms of the conditional probabilities and their ratios ($P > 0.01$). These findings indicate that the motion along linear tracks increases the association and dissociation of CD36 receptors, regardless of whether the receptors are in control or in drug-perturbed cells.

DISCUSSION

The algorithm we present here uses one compact mathematical framework, the linear assignment problem, to first link particles between consecutive frames, and then to close gaps and capture merging and splitting events between the initial track segments. In both steps, particle and track segment assignments are accomplished by spatially global optimization, increasing tracking accuracy under high-particle density conditions. In addition, track segment assignment in the second step is accomplished by temporally global optimization. The combination of these two optimization conditions brings our algorithm close to the theoretically best, yet practically too expensive, multiple-hypothesis tracking approach. Whereas MHT generates tracks by constructing all possible paths starting from particle positions in all frames, our algorithm generates tracks by constructing in the second step all possible paths, starting from the initial track segments obtained in the first step. Starting with track segments substantially reduces the combinatorial space of potential assignments, bringing the solution of the assignment problem into the realm of high-end computing on a state-of-the-art desktop workstation. The price to pay for this reduction in computational complexity is that the initial track segments are generated in a greedy approach, which can lead to irreparable particle assignment errors. However, this limitation can be circumvented by imposing conservative cutoffs on particle assignment in the first step and then rescuing the resulting track interrupts in the second step, which—because of its temporal globality—is less prone to error and can afford wider cutoffs. Thus, by balancing the cutoffs of the first and second assignment steps, our method yields effectively an MHT solution.

The algorithm is highly versatile and applicable to a broad set of tracking tasks in live-cell imaging. We used this framework to track chromosome motion in three dimensions, cell motility in tissue culture, synaptic vesicles and cytoskeleton dynamics (data not shown). Here we showed two applications that highlight two of the most important features of our tracking algorithm. The endocytosis study critically depended on the algorithm's ability to produce complete tracks in dense particle fields, yielding reliable lifetime distributions for all CCPs in the field of view. The CD36 study critically depended on the algorithm's ability to capture merge and split events, and thus reveal the association and dissociation of receptors on a single-molecule level. Both the CCP and the CD36 studies revealed the existence of mechanisms by which a cell might organize the kinetics and dynamics of signal transduction at the level of the plasma membrane. The power of a robust SPT algorithm, in combination with specific molecular interventions, will allow us to uncover the molecular mechanisms underlying this organization in the context of living cells.

METHODS

Software. The tracking software used in this work is available online (**Supplementary Software** online) as well as at http://lccb.scripps.edu/ ('Download' hyperlink) where updated versions may also be available. Software details are available in **Supplementary Note 9** online.

CCP labeling and imaging. We grew and prepared BSC1 (monkey kidney epithelial) cells stably expressing rat brain clathrin light chain–EGFP as specified in **Supplementary Methods** online. For live-cell imaging, we plated BSC1 cells on glass coverslips and performed through-the-objective TIRF microscopy on a Nikon TE2000U inverted microscope using a 100×, 1.45 numerical aperture (NA) oil-immersion objective. We captured images at 0.5 Hz with 200-ms exposure time using a Hamamatsu Orca II-ERG.

CD36 receptor labeling and imaging. We isolated human primary macrophages from human blood samples and cultured them in medium as specified in **Supplementary Methods**. To immunolabel individual CD36 receptors, we incubated cells first with anti-CD36 Fab fragments derived from mouse monoclonal antibodies to human CD36 and then with Cy3-conjugated donkey anti-mouse Fab fragments. We performed live-cell imaging using a Zeiss Axiovert 200 inverted epifluorescence microscope equipped with a 100×, 1.45 NA oil-immersion objective. We captured image streams at 10 Hz for 10 s using an electron-multiplying charge-coupled device (CCD) camera (Hamamatsu).

Additional methods. Details of CCP and CD36 labeling and imaging are available in **Supplementary Methods**.

Note: Supplementary information is available on the Nature Methods website.

ACKNOWLEDGMENTS

This research was supported by the US National Institutes of Health R01 grant GM73165 (to G.D. and S.L.S.), by grants from the Heart and Stroke Foundation of

Canada and the Canadian Institutes for Health Research (to S.G.), and by a postdoctoral fellowship from The Helen Hay Whitney Foundation–The Agouron Institute (to K.J.). We thank T. Kirchhausen (Harvard Medical School) for providing BSC1 cells stably expressing rat brain clathrin light chain–EGFP.

AUTHOR CONTRIBUTIONS

K.J. designed and implemented the tracking algorithm, analyzed CD36 aggregation, and wrote the majority of the manuscript. D.L. analyzed CCP lifetimes and wrote the related sections in the manuscript. M.M. and H.K. acquired live-cell image sequences of clathrin light chain-EGFP and Cy3-Fab fragment–labeled CD36 receptors, respectively. S.G., S.L.S. and G.D. initiated the study and helped edit the manuscript.

Published online at http://www.nature.com/naturemethods/
Reprints and permissions information is available online at http://npg.nature.com/reprintsandpermissions/

1. Sako, Y., Minoguchi, S. & Yanagida, T. Single-molecule imaging of EGFR signalling on the surface of living cells. *Nat. Cell Biol.* **2**, 168–172 (2000).
2. Fujiwara, T., Ritchie, K., Murakoshi, H., Jacobson, K. & Kusumi, A. Phospholipids undergo hop diffusion in compartmentalized cell membrane. *J. Cell Biol.* **157**, 1071–1081 (2002).
3. Groc, L. *et al.* Differential activity-dependent regulation of the lateral mobilities of AMPA and NMDA receptors. *Nat. Neurosci.* **7**, 695–696 (2004).
4. Meijering, E., Smal, I. & Danuser, G. Tracking in molecular bioimaging. *IEEE Signal Process. Mag.* **23**, 46–53 (2006).
5. Kalaidzidis, Y. Intracellular objects tracking. *Eur. J. Cell Biol.* **86**, 569–578 (2007).
6. Ghosh, R.N. & Webb, W.W. Automated detection and tracking of individual and clustered cell-surface low-density-lipoprotein receptor molecules. *Biophys. J.* **66**, 1301–1318 (1994).
7. Crocker, J.C. & Grier, D.G. Methods of digital video microscopy for colloidal studies. *J. Colloid Interface Sci.* **179**, 298–310 (1996).
8. Cheezum, M.K., Walker, W.F. & Guilford, W.H. Quantitative comparison of algorithms for tracking single fluorescent particles. *Biophys. J.* **81**, 2378–2388 (2001).
9. Goulian, M. & Simon, S.M. Tracking single proteins within cells. *Biophys. J.* **79**, 2188–2198 (2000).
10. Schmidt, T., Schutz, G.J., Baumgartner, W., Gruber, H.J. & Schindler, H. Imaging of single molecule diffusion. *Proc. Natl. Acad. Sci. USA* **93**, 2926–2929 (1996).
11. Manley, S. *et al.* High-density mapping of single-molecule trajectories with photoactivated localization microscopy. *Nat. Methods* **5**, 155–157 (2008).
12. Reid, D.B. An algorithm for tracking multiple targets. *IEEE Trans. Automat. Contr.* **24**, 843–854 (1979).
13. Blackman, S.S. & Popoli, R. *Design and Analysis of Modern Tracking Systems*. (Artech House, Norwood, Massachusetts, 1999).
14. Veenman, C.J., Reinders, M.J.T. & Backer, E. Resolving motion correspondence for densely moving points. *IEEE T Pattern Anal.* **23**, 54–72 (2001).
15. Chetverikov, D. & Verestoy, J. Feature point tracking for incomplete trajectories. *Computing* **62**, 321–338 (1999).
16. Shafique, K. & Shah, M. A noniterative greedy algorithm for multiframe point correspondence. *IEEE T Pattern Anal.* **27**, 51–65 (2005).
17. Sbalzarini, I.F. & Koumoutsakos, P. Feature point tracking and trajectory analysis for video imaging in cell biology. *J. Struct. Biol.* **151**, 182–195 (2005).
18. Genovesio, A. *et al.* Multiple particle tracking in 3-D+t microscopy: method and application to the tracking of endocytosed quantum dots. *IEEE Trans. Image Process.* **15**, 1062–1070 (2006).
19. Tvarusko, W. *et al.* Time-resolved analysis and visualization of dynamic processes in living cells. *Proc. Natl. Acad. Sci. USA* **96**, 7950–7955 (1999).
20. Jiang, S., Zhou, X.B., Kirchhausen, T. & Wong, S.T.C. Tracking molecular particles in live cells using fuzzy rule-based system. *Cytometry A* **71A**, 576–584 (2007).
21. Bonneau, S., Dahan, M. & Cohen, L.D. Single quantum dot tracking based on perceptual grouping using minimal paths in a spatiotemporal volume. *IEEE Trans. Image Process.* **14**, 1384–1395 (2005).
22. Genovesio, A. & Olivo-Marin, J.-C. Split and merge data association filter for dense multi-target tracking. *IEEE Int. Conf. Pattern Recognit.* **4**, 677–680 (2004).
23. Racine, V. *et al.* Visualization and quantification of vesicle trafficking on a three-dimensional cytoskeleton network in living cells. *J. Microsc.* **225**, 214–228 (2007).
24. Burkard, K.E. & Cela, E. in *Handbook of Combinatorial Optimization*. Supplement volume A (eds. Du, D. Z. & Pardalos, P. M.) 75–149 (Kluwer Academic Publishers, Dordrecht, The Netherlands, 1999).
25. Jonker, R. & Volgenant, A. A shortest augmenting path algorithm for dense and sparse linear assignment problems. *Computing* **38**, 325–340 (1987).
26. Ehrlich, M. *et al.* Endocytosis by random initiation and stabilization of clathrin-coated pits. *Cell* **118**, 591–605 (2004).
27. Merrifield, C.J., Feldman, M.E., Wan, L. & Almers, W. Imaging actin and dynamin recruitment during invagination of single clathrin-coated pits. *Nat. Cell Biol.* **4**, 691–698 (2002).
28. Rappoport, J.Z. & Simon, S.M. Real-time analysis of clathrin-mediated endocytosis during cell migration. *J. Cell Sci.* **116**, 847–855 (2003).
29. Merrifield, C.J., Perrais, D. & Zenisek, D. Coupling between clathrin-coated-pit invagination, cortactin recruitment, and membrane scission observed in live cells. *Cell* **121**, 593–606 (2005).
30. Olivo-Marin, J.-C. Extraction of spots in biological images using multiscale products. *Pattern Recognit.* **35**, 1989–1996 (2002).
31. Conner, S.D. & Schmid, S.L. Regulated portals of entry into the cell. *Nature* **422**, 37–44 (2003).
32. Macia, E. *et al.* Dynasore, a cell-permeable inhibitor of dynamin. *Dev. Cell* **10**, 839–850 (2006).
33. Febbraio, M., Hajjar, D.P. & Silverstein, R.L. CD36: a class B scavenger receptor involved in angiogenesis, atherosclerosis, inflammation, and lipid metabolism. *J. Clin. Invest.* **108**, 785–791 (2001).
34. Thomann, D., Rines, D.R., Sorger, P.K. & Danuser, G. Automatic fluorescent tag detection in 3D with super-resolution: application to the analysis of chromosome movement. *J. Microsc.* **208**, 49–64 (2002).